

# A Phaseless Inverse Source Method (PISM) Based on Near-Field Scanning for Radiation Diagnosis and Prediction of PCBs

Lixiao Wang, Yuxian Zhang<sup>ID</sup>, *Student Member, IEEE*, Feng Han<sup>ID</sup>, *Senior Member, IEEE*, Jianyang Zhou<sup>ID</sup>, *Member, IEEE*, and Qing Huo Liu<sup>ID</sup>, *Fellow, IEEE*

**Abstract**—In this article, we present an efficient phaseless inverse source method (PISM) to reconstruct equivalent sources on a printed circuit board (PCB) using magnitude-only single-plane near-field scanning. The equivalent source distribution reconstructed by the conventional source reconstruction method requires accurate near-field magnitude and phase information, but phase measurement is difficult in many cases due to inaccuracy and complexity. In order to describe the inverse problem between phaseless fields and radiation sources, a nonlinear cost function based on surface integral equations is established. The cost function of the PISM is rapidly minimized by an iterative optimization and regularization technique for nonlinear ill-posed systems. The proposed method gives the characterization of PCBs both for diagnostic tasks of radiation sources and the near-field radiation behavior prediction when the phase information is missing. It also shows excellent robustness in tackling with various near-field data and noises. Both numerical examples and laboratory experiments are given to verify the effectiveness of the proposed method.

**Index Terms**—Integral equations, near-field scanning, phaseless inverse source method (PISM), printed circuit board (PCB), source reconstruction method (SRM).

## I. INTRODUCTION

WITH the increase of working frequencies, signal integrity and power integrity of integrated circuits (ICs) have become an important research issue. The conduction noise and radiation noise produced by a printed circuit board (PCB) may cause electromagnetic interferences to its own circuits and surrounding circuits [1], [2]. Most of the

Manuscript received December 30, 2019; revised April 12, 2020 and June 12, 2020; accepted June 21, 2020. Date of publication July 30, 2020; date of current version October 5, 2020. This work was supported in part by the National Natural Science Foundation of China under Grant 61871462 and in part by the National Key R&D Program of the Ministry of Science and Technology of China under Grant 2018YFC0603503. (*Corresponding authors:* Qing Huo Liu; Jianyang Zhou.)

Lixiao Wang and Feng Han are with the Fujian Provincial Key Laboratory of Electromagnetic Wave Science and Detection Technology, Institute of Electromagnetics and Acoustics, Xiamen University, Xiamen 361005, China (e-mail: feng.han@xmu.edu.cn).

Yuxian Zhang is with the Institute of Microscale Optoelectronics, Shenzhen University, Shenzhen 518060, China (e-mail: yxzheng\_tute@126.com).

Jianyang Zhou is with the Department of Electronic Engineering, Xiamen University, Xiamen 361005, China (e-mail: zhoujy@xmu.edu.cn).

Qing Huo Liu is with the Department of Electrical and Computer Engineering, Duke University, Durham, NC 27708 USA (e-mail: qhliu@duke.edu).

Color versions of one or more of the figures in this article are available online at <http://ieeexplore.ieee.org>.

Digital Object Identifier 10.1109/TMTT.2020.3006564

manufactured electronic products must be tested by a professional electromagnetic compatibility (EMC) testing organization before entering the market. Engineers need to strictly control various circuit parameters to limit noises produced by their electronic products [3]. Hence, it is of great significance for engineers to find radiation sources in PCBs and predict the radiation behaviors of PCBs.

In recent years, near-field scanning devices have been used to diagnose radiation sources in PCBs [4]. It is the most direct and simplest way to locate radiation sources through the scanned near-field results. However, in order to achieve higher accuracy, smaller stepping motor devices, smaller diameter probes, lower scanning plane, and longer scanning time are needed [5], [6]. Based on near-field scanning, the source reconstruction method (SRM) originally used in antenna diagnosis has been applied to radiation diagnosis and prediction of PCBs [7], [8].

The conventional SRM can be described as follows. First, magnetic and/or electric fields above the device under test (DUT) are collected by a near-field scanning device. The conventional SRM minimizes the measured fields and the simulated radiation fields of the equivalent current to determine the distribution of the equivalent current. Then, the equivalent current can be used to calculate radiation fields at any point in space. The conventional SRM requires magnitude and phase information of magnetic and/or electric fields to reconstruct the accurate equivalent source distribution [9]–[13]. In previous studies for antenna diagnostics, fields on two scanning planes at different distances are used to retrieve the phase information. This phase retrieved method is based on two scanning planes with a sufficient distance, which results in a significant phase change between the two scanning planes [14], [15]. However, this phase retrieval method cannot be effectively applied to the phase retrieval of ICs such as dc–dc converters and clock circuits because the wavelength of radiation sources in such applications is usually much longer than the distance between two scanning planes [16].

In [17], two-phase measurement methods with a combination of a measuring probe and a reference probe are proposed for near-field scanning. For the first method, a spectrum analyzer is replaced by a vector network analyzer (VNA), which is set to the external source mode. For the second method, only a spectrum analyzer is required, but three scans

are required and an additional  $180^\circ$  hybrid circuit is introduced. More complex operations and longer scanning time are common disadvantages of the abovementioned approaches [18], [19]. Compared with the phase measurement, the phaseless measurement is simpler and less limited.

The conventional SRM using magnitude and phase near-field information is a linear ill-posed system. In contrast, the SRM without phase leads to a nonlinear system. In [20] and [21], the researchers use electric or magnetic dipoles as equivalent radiation sources. Due to the absence of phase information, global optimization algorithms, such as the genetic algorithm and the differential evolution algorithm, are applied to solve the nonlinear system. Some researchers combine the genetic algorithm and the least-squares (LSQ) method to reduce the computation cost of the genetic algorithm [22]. However, the approach of global optimization algorithms is still limited if the PCB is very complex and many dipoles are needed.

For inverse problems, the iterative method is powerful for a large number of unknowns and becomes a suitable approach for solving the distribution of equivalent sources. In [19] and [23], these iterative methods often required two scanning planes and the phase information is iterated over and over between two scanning planes. Some researchers have also studied source reconstruction in time domain [24], [25]. In recent years, machine learning and neural networks are used as new tools for near-field diagnosis and prediction [26], [27].

In this article, we propose an efficient phaseless inverse source method (PISM), which determines the distribution of equivalent radiation sources from magnitude-only and single-plane near-field scanning. The inspiration for our method comes from the Born iterative method (BIM) that has been successfully applied to the nonlinear inverse scattering problem. The cost function for the nonlinear system is solved by an iterative method combined with the conjugate gradient (CG) method and it converges stably with the increase of iteration number. To our knowledge, this iterative approach is the first time to be applied to phaseless inverse source problem and only one scanning plane is required. Compared with global optimization algorithms, a large number of unknowns can be solved quickly. The proposed method provides a dependable equivalent radiation source for radiation source diagnosis and near-field simulation of a PCB when phase information is difficult to collect accurately and efficiently.

This article is organized as follows. In Section II, the theory and formulation of the proposed method are presented. In Section III, the validity and accuracy of the proposed method are verified by numerical experiments. In Section IV, the effects of noise and near-field sampling distance on the proposed method are analyzed. In Section V, a dc–dc buck converter and an RF amplifier are analyzed to further verify the proposed method.

## II. FORMULATION

### A. Forward Problem

The near-field radiation behavior of a PCB will become a complex problem if we consider the structure of the PCB and encapsulation of electronic devices. For a typical PCB,

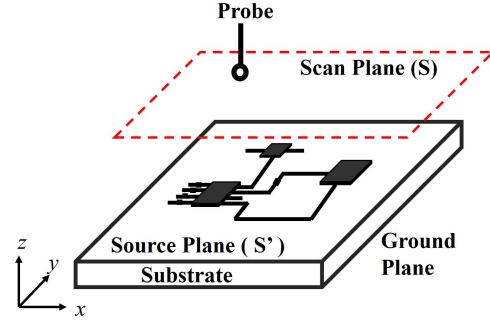


Fig. 1. Illustration of near-field scanning above a PCB.

there is a ground plane mounted on the bottom. A substrate above the ground plane will be welded with some traces and circuit elements on the top surface, which may be identified as radiation sources of the PCB. This radiation problem can be simplified for several reasons: The thickness of the substrate above the ground plane is sufficiently small relative to the wavelength at the operating frequency. For example, a 1-mm-thick substrate is only 1/300 wavelength at 1 GHz. Therefore, the effect of the substrate on radiated fields is negligible. For a finite ground plane of the PCB, the total fields above the PCB consist of the direct term, the mirror term, and the diffraction term. If the near-field scanning is performed on a plane close enough to the PCB, the diffraction term is so weak that the direct and image term can approximate total near fields well. Therefore, the finite ground plane of a PCB can be assumed as an infinite ground plane. The electromagnetic image theory can be applied in the process of radiation source reconstruction. Thus, a simplified model considered in this article is a half-space radiation model [27]. If the thickness and dielectric of the substrate have nonnegligible effects on fields, a more rigorous model (perhaps a layered medium) should be considered.

According to the electromagnetic equivalence principle, radiation sources of the PCB can be made equivalent to either electric current or magnetic current sources or a combination of both. Therefore, different kinds of equivalent models are possible to be selected [28]. Considering the actual situation, many backflow currents forming current loops and magnetic devices can be equivalent to magnetic current sources. Therefore, we consider that magnetic currents to replace this real radiation sources of PCBs in this article, although the formulation is also applicable to electric current sources [29], [30].

For generality, we assume that we have no prior information except the geometrical dimensions of the PCB known in advance. With reference to Fig. 1, the source surface  $S'$  has a distance equal to the thickness of the substrate to the ground plane. The surface  $S$  denotes the near-field scanning plane and is located above the source surface  $S'$ . In the Cartesian coordinates, the ground plane is placed at  $z = 0$ . In order to obtain sufficient electric and magnetic field information, the scanning plane is assumed to be large enough to contain almost all the radiation generated by the radiation source in the PCB. In the proposed PISM, we employ electric field ( $\mathbf{E}$ ) and magnetic field ( $\mathbf{H}$ ) surface magnetic current integral

equations to calculate electric fields and magnetic fields in the scanning plane  $S$  above the PCB. If the source is equivalent to the electric current source, magnetic current integral equations should be transformed to electric current integral equations.

In the half-space with a ground plane at  $z = 0$ , the electric field ( $\mathbf{E}$ ) and magnetic field ( $\mathbf{H}$ ) at  $\mathbf{r} = (x, y, z)$  can be expressed as follows:

$$\mathbf{H} = \frac{-j}{\omega\mu_0} [k_0^2 + \nabla\nabla \cdot] \int_{S'} [g_1(\mathbf{r}, \mathbf{r}') \mathbf{M}(\mathbf{r}')] + g_2(\mathbf{r}, \mathbf{r}') \mathbf{M}_I(\mathbf{r}') dS' \quad (1)$$

$$\mathbf{E} = -\nabla \times \int_{S'} [g_1(\mathbf{r}, \mathbf{r}') \mathbf{M}(\mathbf{r}') + g_2(\mathbf{r}', \mathbf{r}') \mathbf{M}_I(\mathbf{r}') dS' \quad (2)$$

$$g_1(\mathbf{r}, \mathbf{r}') = \frac{e^{-jkR}}{R} \quad (3a)$$

$$g_2(\mathbf{r}, \mathbf{r}') = \frac{e^{-jkR_I}}{R_I} \quad (3b)$$

where  $\mathbf{M}(\mathbf{r}')$  represents the real surface magnetic current located at  $\mathbf{r}' = (x', y', z')$  and  $\mathbf{M}_I(\mathbf{r}')$  is the image magnetic current obtained via the image theory located at  $\mathbf{r}'_I = (x', y', -z')$  [31]. The value of  $k$  is the wavenumber of the propagating medium, and  $\mu_0$  is the permeability of vacuum. The source plane  $S'$  is discretized uniformly by a rectangular grid.  $\mathbf{M}(\mathbf{r}')$ ,  $\mathbf{M}_I(\mathbf{r}')$ ,  $R$ , and  $R_I$  are defined as follows:

$$\mathbf{M}(\mathbf{r}') = \hat{x}M_x(\mathbf{r}') + \hat{y}M_y(\mathbf{r}') + \hat{z}M_z(\mathbf{r}') \quad (4a)$$

$$\mathbf{M}_I(\mathbf{r}') = \hat{x}M_x(\mathbf{r}'_I) + \hat{y}M_y(\mathbf{r}'_I) - \hat{z}M_z(\mathbf{r}'_I) \quad (4b)$$

$$R = \sqrt{(x - x')^2 + (y - y')^2 + (z - z')^2} \quad (5a)$$

$$R_I = \sqrt{(x - x')^2 + (y - y')^2 + (z + z')^2}. \quad (5b)$$

The integration in (1) and (2) can be written in a simpler form using the half-space dyadic Green's functions

$$\mathbf{H} = \int_{S'} \mathbf{G}^{HM}(\mathbf{r}, \mathbf{r}') \mathbf{M}(\mathbf{r}') dS' \quad (6)$$

$$\mathbf{E} = \int_{S'} \mathbf{G}^{EM}(\mathbf{r}, \mathbf{r}') \mathbf{M}(\mathbf{r}') dS' \quad (7)$$

where  $\mathbf{G}^{EM}$  and  $\mathbf{G}^{HM}$  are the electric and magnetic dyadic Green's functions for the half-space, respectively [32].

### B. Inverse Problem

In practice, near-field scanning data can be collected by an electric or a magnetic probe moving on a scanning plane close to the PCB. According to (6) and (7), the unknown magnetic current source can be solved by electric or magnetic fields or some combination of them on the scanning plane. We use a linear operator  $\mathbf{P}$  to represent a linear combination of electric and magnetic fields

$$\mathbf{f} = \mathbf{P} \begin{bmatrix} \mathbf{E} \\ \eta \mathbf{H} \end{bmatrix} = \mathbf{PGM} = \mathbf{BM} \quad (8)$$

where  $\mathbf{P}$  is an  $N_c \times 6$  matrix ( $N_c$  is the number of field components used) and  $\mathbf{f}$  is the measured fields for inversion. By solving the linear system (8), the conventional SRM determines the distribution of the equivalent magnetic current

$\mathbf{M}$ .  $\mathbf{M}$  is composed of  $M_x$ ,  $M_y$ , and  $M_z$ . The notation  $|M|$  denotes the magnitude of  $\mathbf{M}$  and is given as follows:

$$|M| = \sqrt{|M_x|^2 + |M_y|^2 + |M_z|^2}. \quad (9)$$

In the above,  $\eta$  is a scaling factor for balancing the order of magnitude of  $E$  and  $H$  fields.  $\mathbf{GM}$  is defined as follows:

$$\mathbf{GM} = \left[ \eta \int_{S'} \mathbf{G}^{EM}(\mathbf{r}, \mathbf{r}') \mathbf{M}(\mathbf{r}') dS' \right] \quad (10)$$

and

$$\mathbf{B} = \mathbf{PG}. \quad (11)$$

Based on (8), the electric field, magnetic field, or a combination of any of their components can be used as the measured field data for the inverse problem. Naturally, this depends on which type of probe is more suitable for the real measurement. Compared with a magnetic field probe, an efficient electric field probe is usually more difficult to design and manufacture at a lower frequency [33]. In this article, tangential components of the magnetic field  $H_x$  and  $H_y$  collected by the near-field scanning equipment are applied as input data to determine the equivalent magnetic current distribution. Therefore,  $\mathbf{P}$  is chosen as follows:

$$\mathbf{P} = \begin{bmatrix} 0 & 0 & 0 & 0 & 0 & 0 \\ 0 & 0 & 0 & 1 & 1 & 0 \end{bmatrix}. \quad (12)$$

If the near-field scanning equipment collects both the magnitude and phase of a field, (8) will be considered as a linear system. For a well-conditioned linear problem, the result can be obtained by directly solving linear equations [9]. However, the problem we deal with is ill-posed in most cases. Considering the ill-posed problem, constraints or regularization techniques are required in order to obtain a reasonable solution close to the true solution. Based on the LSQ idea and the regularization technique, the cost function  $F$  for this linear ill-posed system is defined as

$$F(\mathbf{M}) = \frac{\|\mathbf{f} - \mathbf{BM}\|^2}{\|\mathbf{f}\|^2} + \gamma^2 \frac{\|\mathbf{M}\|^2}{\|M_c\|^2} \quad (13)$$

where  $\|\cdot\|$  denotes the  $L_2$  norm and  $\mathbf{M}$  is the solution that minimizes the cost function and is normalized by the constant  $M_c$ .  $M_c$  should be a value that is approximate to the norm value of the true solution. The regularization parameter  $\gamma$  should be set to a number within a reasonable range. The method to choose the value of  $\gamma$  can be referred to [34].

Acquired fields with magnitude and phase information make it feasible to solve the linear ill-posed system and obtain the equivalent magnetic current of the PCB [9]. However, phase measurements are difficult to carry out in many cases. Then, utilizing magnitude-only near-field scanning data to reconstruct the equivalent source becomes a preferred method. Therefore, the quantity to be minimized is related to the difference between the magnitude of a field calculated by the equivalent magnetic current and the measured field components [35]. For the magnitude-only case, separating the real part and the imaginary part, the cost function (12) can be

converted to

$$F(\tilde{\mathbf{M}}) = \frac{\| |\mathbf{f}| - \sqrt{(\mathbf{B}_1 \tilde{\mathbf{M}})^2 + (\mathbf{B}_2 \tilde{\mathbf{M}})^2} \|_2^2}{\| |\mathbf{f}| \|_2^2} + \gamma^2 \frac{\| \tilde{\mathbf{M}} \|_2^2}{\| M_c \|_2^2} \quad (14)$$

$$\tilde{\mathbf{M}} = \begin{bmatrix} \text{Re}(\mathbf{M}) \\ \text{Im}(\mathbf{M}) \end{bmatrix} \quad (15)$$

$$\mathbf{B}_1 = \begin{bmatrix} \text{Re}(\mathbf{B}) & -\text{Im}(\mathbf{B}) \end{bmatrix} \quad (16a)$$

$$\mathbf{B}_2 = \begin{bmatrix} \text{Im}(\mathbf{B}) & \text{Re}(\mathbf{B}) \end{bmatrix} \quad (16b)$$

where special attention must be paid to the numerator of the first term of the cost function: Here,  $|\mathbf{f}|$  and  $|\mathbf{f}^s| \equiv ((\mathbf{B}_1 \tilde{\mathbf{M}})^2 + (\mathbf{B}_2 \tilde{\mathbf{M}})^2)^{1/2}$ , respectively, denote the vectors of measured and simulated element-by-element modulus of the field rather than the magnitude of the whole field vector [36]. Equation (13) is related to a linear ill-posed system, whereas (14) leads to a nonlinear ill-posed system.

In geophysical exploration and biomedical imaging, the BIM is an effective and convergent method for solving the nonlinear inverse scattering problem [37]. Inspired by the BIM, the solution  $\tilde{\mathbf{M}}$  can be found by minimizing the function (14), i.e., by letting the derivative of  $F$  with respect to  $\tilde{\mathbf{M}}$  to be zero to arrive at

$$\frac{\mathbf{A}\tilde{\mathbf{M}}}{\| |\mathbf{f}| \|_2^2} + \gamma^2 \frac{\tilde{\mathbf{M}}}{\| M_c \|_2^2} = \frac{\mathbf{c}(\tilde{\mathbf{M}})}{\| |\mathbf{f}| \|_2^2} \quad (17)$$

$$\mathbf{A} = \begin{bmatrix} \text{Re}(\mathbf{B})^T \mathbf{B}_1 + \text{Im}(\mathbf{B})^T \mathbf{B}_2 \\ -\text{Im}(\mathbf{B})^T \mathbf{B}_1 + \text{Re}(\mathbf{B})^T \mathbf{B}_2 \end{bmatrix} \quad (18)$$

$$\mathbf{c}(\tilde{\mathbf{M}}) = \begin{bmatrix} \mathbf{B}_1 \\ \mathbf{B}_2 \end{bmatrix}^T \left[ \text{diag}(\mathbf{B}_1 \tilde{\mathbf{M}}) \mathbf{D}(\tilde{\mathbf{M}}) |\mathbf{f}| \right] \quad (19a)$$

$$\mathbf{D}(\tilde{\mathbf{M}}) = \text{diag}(\sqrt{(\mathbf{B}_1 \tilde{\mathbf{M}})^2 + (\mathbf{B}_2 \tilde{\mathbf{M}})^2})^{-1} \quad (19b)$$

where  $\text{diag}(\cdot)$  denotes the transformation of a column vector into a diagonal matrix. The nonlinear equation (17) can be solved iteratively for the  $(n+1)$ th iteration as follows:

$$\left( \frac{\mathbf{A}}{\| |\mathbf{f}| \|_2^2} + \frac{\gamma^2}{\| \tilde{\mathbf{M}}^{(n)} \|_2^2} \mathbf{I} \right) \tilde{\mathbf{M}}^{(n+1)} = \frac{\mathbf{c}(\tilde{\mathbf{M}}^{(n)})}{\| |\mathbf{f}| \|_2^2} \quad (20)$$

where  $\tilde{\mathbf{M}}^{(n)}$  denotes the result of the  $n$ -th iteration and  $\mathbf{I}$  is the identity matrix [38]. This linearization step assumes a slow change in the nonlinear term on the right-hand side of (17). It is found to work well in all our examples. The linear system (20) can be solved by the CG method [39]. The initial  $\tilde{\mathbf{M}}^{(0)}$  can be directly estimated or calculated by solving (13) with zero phase information. The solution  $\tilde{\mathbf{M}}$  will be updated iteratively until the cost function reaches an acceptable misfit or the procedure reaches its maximum iteration number.

In order to check the accuracy of the method, the following relative data error (RDE) is computed:

$$\text{RDE} = \frac{\| \sqrt{(\mathbf{B}_1 \tilde{\mathbf{M}}^{(n)})^2 + (\mathbf{B}_2 \tilde{\mathbf{M}}^{(n)})^2} - |\mathbf{f}| \|}{\| |\mathbf{f}| \|}. \quad (21)$$

### III. NUMERICAL EXAMPLES AND VALIDATION

In this section, we validate the proposed PISM by considering the radiated fields of an L-shaped microstrip line. The physical dimensions of the PCB and position of the line are shown in Fig. 2. The PCB is an  $80 \text{ mm} \times 80 \text{ mm} \times 1 \text{ mm}$

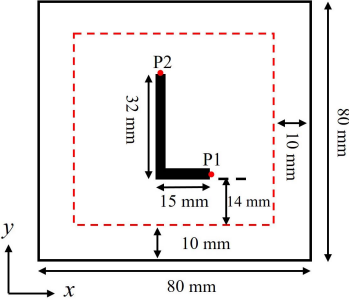


Fig. 2. Schematic and dimensions of an L-shaped microstrip line on a PCB.

board located on the  $xy$  plane at  $z = 0 \text{ mm}$ . A 2-mm-wide L-shaped microstrip line is located on the top of the board, whereas a ground plane is at the bottom of the board. The relative permittivity and loss tangent of the dielectric substrate are 4.7 and 0.025, respectively. At one end P1, the microstrip is excited by a voltage source of 1 V with a source impedance of  $50 \Omega$ , while a  $50\Omega$  load is applied to terminate the microstrip at the other end P2.

In Fig. 2, a  $60 \text{ mm} \times 60 \text{ mm}$  scanning plane is marked by red lines at a height of 10 mm above the ground plane of the PCB. The near magnetic field at 1 GHz over the scanning plane is simulated by a full-wave solver [40]. The near-field sampling interval on the scanning plane is 2 mm in both  $x$ - and  $y$ -directions ( $\Delta x = \Delta y = 2 \text{ mm}$ ), and then, the total number of sampling points is  $31 \times 31 = 961$ . The simulated near-field data is applied as reference data in this example. The equivalent magnetic current is reconstructed over the PCB surface ( $z = 1 \text{ mm}$ ). We assume that the physical model of radiation sources is unknown, and hence, the area of the equivalent magnetic current is set to  $60 \text{ mm} \times 60 \text{ mm}$  and is divided into  $30 \times 30 = 900$  elements by a square grid with an element length of 2 mm. This step size is chosen to make the element smaller than both the wavelength and the board's main components to have a fine resolution.

The equivalent magnetic current is reconstructed by  $|H_x|$  and  $|H_y|$  on the scanning plane ( $z = 10 \text{ mm}$ ). Once the equivalent magnetic current is determined, near fields in space can be calculated. Fig. 3 shows the comparison of the magnitude of magnetic fields on a higher plane ( $z = 15 \text{ mm}$ ) generated by the full-wave solver and the proposed method. The results of the full-wave solver and the equivalent magnetic current agree well. Here, we define the error  $\sigma$  and error in dB  $\sigma_{\text{dB}}$  of field, i.e.,  $|H_x|$  as follows:

$$\sigma = \frac{\sqrt{\sum_{i=1}^a \sum_{j=1}^b (|H_x^{\text{re}}(i, j)| - |H_x^{\text{mea}}(i, j)|)^2}}{\sqrt{\sum_{i=1}^a \sum_{j=1}^b (|H_x^{\text{mea}}(i, j)|)^2}} \quad (22)$$

$$\sigma_{\text{dB}} = 20 \log_{10} \sigma \quad (23)$$

where  $|H_x^{\text{re}}|$  and  $|H_x^{\text{mea}}|$  denote reconstructed and measured  $|H_x|$ , respectively. The values of  $a$  and  $b$  represent the number of sampling points in the  $x$ - and  $y$ -directions. The errors  $\sigma$  and  $\sigma_{\text{dB}}$  of  $|H_x|$  and  $|H_y|$  in Fig. 3 are 5.8% and 7.2%, -24.73 and -22.85 dB, respectively.

As shown in Fig. 4(a), the synthetic equivalent magnetic current  $|M|$  obtained by the proposed PISM has a high

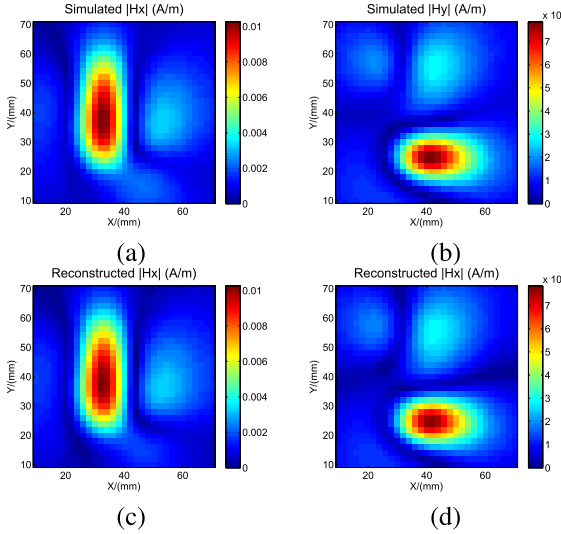


Fig. 3. Comparison between the magnetic fields at 1 GHz in the higher plane ( $z = 15$  mm) generated by the full-wave solver and the equivalent magnetic current source for the L-shaped microstrip line. (a) and (b) Simulated  $|H_x|$  and  $|H_y|$ . (c) and (d) Reconstructed  $|H_x|$  and  $|H_y|$ .

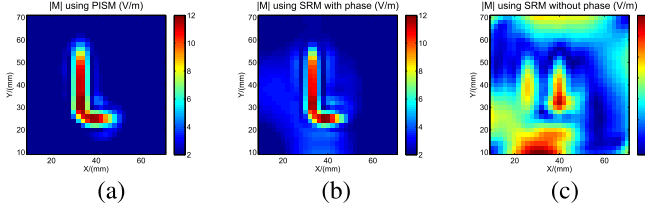


Fig. 4. Equivalent magnetic current  $|M|$  distribution over the PCB surface for the L-shaped microstrip line obtained by using (a) proposed PISM without phase, (b) conventional SRM with phase, and (c) conventional SRM without phase.

resolution and is distributed along the L-shape microstrip line. Moreover, Fig. 4(a) is in good agreement with the result of the conventional SRM with phase shown in Fig. 4(b), whereas the result of conventional SRM without phase is poor. This indicates that the proposed PISM provides an efficient source distribution for locating radiation sources when the phase information is missing.

Then, we further analyze the component  $M_x$  obtained by the proposed PISM and the conventional SRM with phase. As shown in Fig. 5, the magnitude of  $M_x$  obtained by the proposed PISM has good consistency with the result of the conventional SRM with phase. For the phase information of  $M_x$ , if we assume that the results of the SRM with phase are the “true solution,” there is a slight phase deviation due to the missing phase information in the inverse problem. However, a slight phase deviation will not affect the accuracy of the near-field prediction of PCBs, as shown in Fig. 3.

In order to show the convergence of the proposed PISM, the RDE curve is plotted in Fig. 6. It can be clearly observed that as the number of iterations increases, the RDE gradually decreases and finally terminates at 4%.

#### IV. ANALYSIS OF NOISE AND NEAR-FIELD SCANNING RESOLUTION

In this section, the noise and the sampling interval in the near-field scanning are our focuses. Similar to the L-shaped

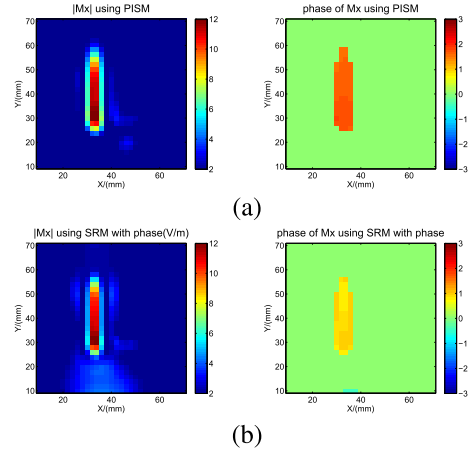


Fig. 5. Magnitude and phase of  $M_x$  distribution over the PCB surface for the L-shaped microstrip line obtained by using (a) PISM without phase and (b) conventional SRM with phase.

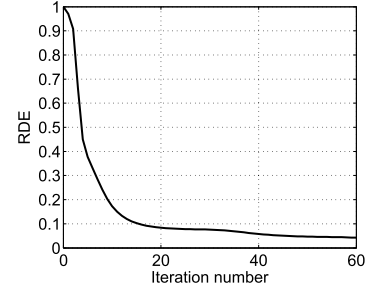


Fig. 6. RDE versus iteration number for the L-shaped microstrip line.

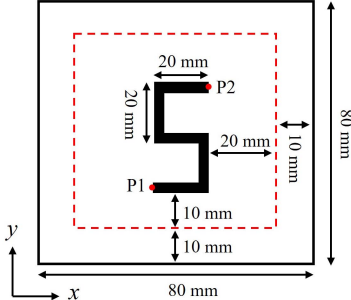


Fig. 7. Schematic and dimensions of an S-shaped microstrip line on a PCB.

microstrip line, an S-shaped microstrip line is taken as an example. Except for the size of microstrip line, other parameters, including the scanning parameters, are the same as the L-shaped microstrip line case. The height of the scanning plane is 10 mm ( $z = 10$  mm). The dimensions of the S-shaped microstrip line are shown in Fig. 7.

In order to simulate measurement noises, white Gaussian noises with different power levels are added to the magnitude distribution of the magnetic field on the scanning plane ( $z = 10$  mm). In this case, the signal-to-noise ratio (SNR) of near-field data is specified as 30, 20, 15, and 10 dB. The sampling distance is set to 2 mm ( $\Delta x = \Delta y = 2$  mm) for all scanning data. Fig. 8 shows equivalent magnetic currents with different noise levels calculated by the proposed method.

As shown in Fig. 8, the equivalent magnetic current can still be reconstructed accurately as the SNR decreases. Because of noises, some clutters appear in the reconstructed results.

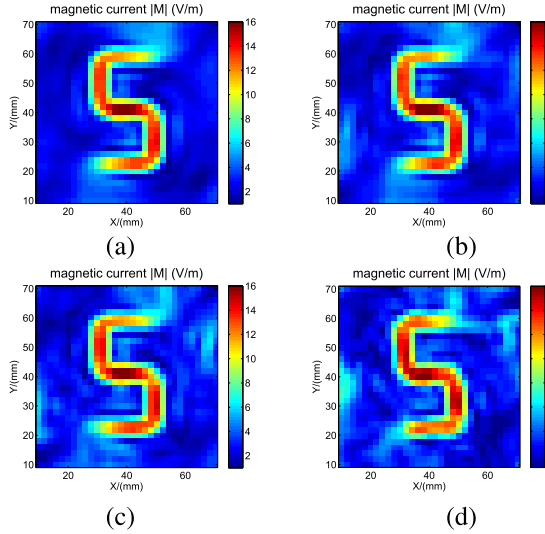


Fig. 8. Equivalent magnetic current  $|M|$  distribution for the S-shaped microstrip line from the scanning data with different noise level. (a) SNR = 30 dB. (b) SNR = 20 dB. (c) SNR = 15 dB. (d) SNR = 10 dB.

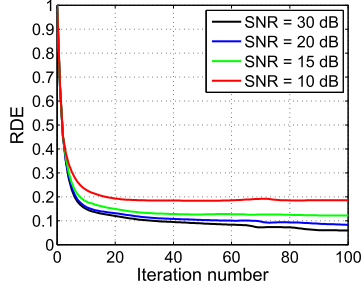


Fig. 9. RDE versus iteration number for the S-shaped microstrip line.

From the RDE curve shown in Fig. 9, we can see that the final stable relative error of the proposed method increases as the SNR decreases. In these four cases, the RDE converges to 6%, 8%, 12%, and 18.5%, respectively. These results show the good noise robustness of the proposed PISM.

In order to study the influence of the sampling interval on the proposed method, the SNR is set to 30 dB and unchanged in the following cases to highlight the influence of the sampling interval. For comparison, 2-, 3-, 4-, and 5-mm sampling intervals are used. In these four cases, the number of unknowns of the magnetic current source remains constant. It should be pointed out that when the sampling interval is set to 2, 3, 4, and 5 mm, i.e., the number of near-field data is 1922, 882, 512, and 338.

The equivalent magnetic current calculated by the proposed PISM is shown in Fig. 10. With the increase of sampling interval, (8) becomes more underdetermined and the difficulty of solving the nonlinear system also increases. It can be seen that the proposed PISM reconstructs equivalent magnetic current sources accurately except when the sampling interval is 5 mm. For Fig. 9(d), the number of near-field data is only 338, and thus, it is difficult to obtain a good solution in the inverse problem. By comparing Fig. 9(a)–(c), when the sampling interval is 2 mm, the total number of near-field data is 1922, which is 3.75 times the amount of data with a 4-mm sampling interval. It shows that the proposed PISM has good robustness in terms of the amount of measured data.

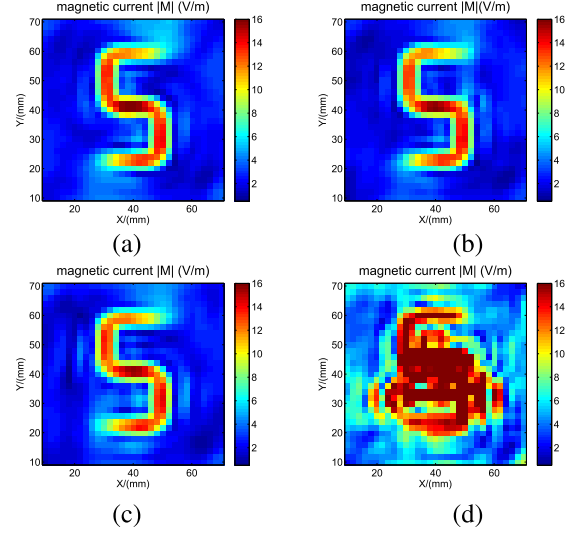


Fig. 10. Equivalent magnetic current  $|M|$  distribution for the S-shaped microstrip line from the scanning data with different sampling distance. (a) 2 mm. (b) 3 mm. (c) 4 mm. (d) 5 mm.

## V. LABORATORY EXPERIMENT

### A. Discussion About Parameters of Scanning

In this article, some parameters, including the scan plane size, plane height, and sampling interval, are discussed for near-field measurements. The plane size is related to the plane height. If the plane height increases with the plane size unchanged, the smaller viewing angle of the scan plane will mean less field information collected. We suggest that a larger scanning plane will obtain more field information. However, it is large enough if the field pattern can contain almost field values above  $-40$  dB to  $-30$  dB (compared with the maximum field peak).

The sampling interval is also related to the plane height. In general, the lower the plane height, the faster the field changes spatially. Hence, the probe density should increase to ensure the complete field information. A sampling criterion is proposed in [41]. The relationship among the sampling intervals  $\Delta x$ ,  $\Delta y$ , wavelength  $\lambda$ , and scan height  $h$  is shown in the following:

$$\Delta x, \Delta y \leq \frac{\lambda}{2\sqrt{1 + (\frac{\lambda}{h})^2}}. \quad (24)$$

Therefore, the abovementioned scanning parameters should be weighed in the near-field measurement.

In our laboratory experiment, near-field data are collected by a magnetic probe with a coil diameter of 2 mm. Fig. 11 shows the configuration of the phaseless near-field scanning equipment. A spectrum analyzer is used as a receiver and is connected to the near-field magnetic probe by a coaxial cable. The induced voltage of the near-field probe is corrected by the IEC61967-6 standard to obtain the correct magnetic field value at the probe position [4], [42], [43]. A six-axis robot with a  $20\text{-}\mu\text{m}$  motor stepping is used for computer commands to move the magnetic probe.

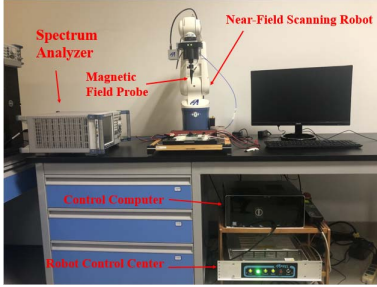


Fig. 11. Setup for the phaseless near-field scanning measurement.

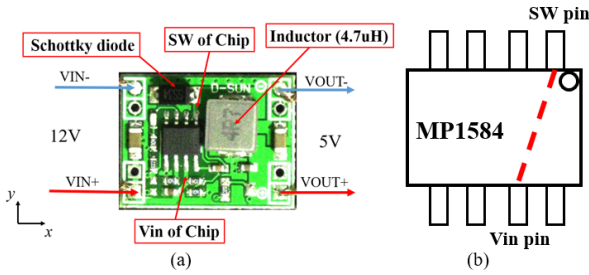


Fig. 12. (a) Top view of dc-dc buck converter. (b) MP1584 chip.

### B. DC-DC Buck Converter based on MP1584 Chip

In all electronic systems, the power supply is the most basic module. There are many electronic systems using a switching power supply, which often becomes a radiation source in the near field. Radiation frequencies of a dc-dc buck converter range from a few kilohertz to a few tens of megahertz. In this article, a dc-dc buck converter with an input voltage of 12 V and an output voltage of 5 V is used as the DUT to verify the proposed method in the laboratory. Fig. 12(a) shows a photograph of a PCB containing the dc-dc buck converter. The length and width of the PCB are 21.5 and 16.5 mm, respectively.

This dc-dc buck converter is mainly controlled by an MP1584 chip, which has metal-oxide-semiconductor field-effect transistor (MOSFET) built-in and works in the pulsedwidth modulation (PWM) mode. The switching frequency  $f_s$  of MP1584 chip is set by an external resistor  $R_{\text{freq}}$  from FREQ pin to ground. The value of  $R_{\text{freq}}$  can be calculated from

$$R_{\text{freq}}(\text{k}\Omega) = \frac{180000}{f_s(\text{kHz})^{1.1}}. \quad (25)$$

In this article,  $R_{\text{freq}}$  is set to 100 kΩ, so the switching frequency is approximately 910 kHz.

There are two important pins on this chip, Vin and SW. The input of Vin is dc 12 V and the output of SW is the switch voltage. The path from Vin to SW is the main current path shown in Fig. 12(b). The time-domain switch voltage is measured by an Agilent oscilloscope and shown in Fig. 13. It can be found that high-frequency components of switch voltage are produced on the rising and falling stages of the voltage. After the near-field measurement, we select two typical frequencies, 960 kHz and 36.2 MHz, which represent the fundamental frequency and higher harmonic of the switching frequency of the converter. The scanning plane (30 mm × 30 mm) is set at  $z = 6.5$  mm with 1-mm sampling interval ( $\Delta x = \Delta y = 1$  mm).

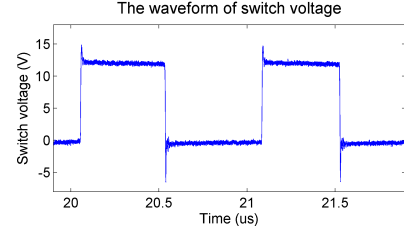


Fig. 13. Waveform of switch voltage measured by the Agilent oscilloscope.

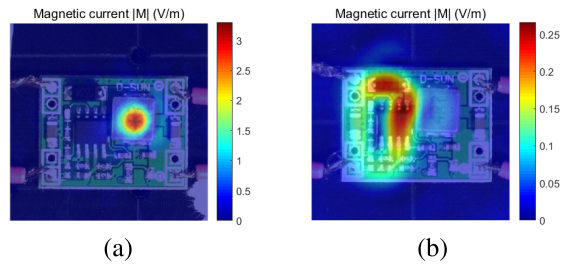


Fig. 14. Equivalent magnetic current  $|M|$  distribution for the dc-dc buck converter from the scanning plane data ( $z = 6.5$  mm). (a) 960 kHz. (b) 36.2 MHz.

The reconstructed area of the equivalent magnetic current is set equal to the area of scanning plane and is divided into  $30 \times 30 = 900$  elements by a square grid with a side length of 1 mm at  $z = 1$  mm. The equivalent magnetic current obtained by the proposed PISM is shown in Fig. 14.

From Fig. 14(a), we can intuitively find that the radiation hot spot is concentrated at the position of 4.7-μH inductor. The possible reason why the inductor radiation occurs at 960 kHz is that when the switching voltage passes through the inductor, the inductor blocks the high-frequency component of the switching voltage, whereas the low frequency is less affected. From Fig. 14(b), we can see that there are two main radiation devices, MP1584 chip and Schottky diode. A very useful phenomenon is that the equivalent magnetic current distribution on the MP1584 chip has good consistency with the Vin to SW path [the red dotted line shown in Fig. 12(b)]. In addition, the Schottky diode plays an important role in voltage stabilization and electric current continuation. When the voltage changes direction momentarily, the high-frequency voltage passes through the Schottky diode due to the recovery time of diode. This is the reason for the radiation by the Schottky diode.

Then, we use the equivalent magnetic current to predict the distribution of the magnetic field on a higher plane ( $z = 11.5$  mm). The measured fields and reconstructed fields are compared in Figs. 15 and 16. A comparison of the results measured by the near-field scanner and predicted by the proposed method verifies the good agreement. The errors  $\sigma$  and  $\sigma_{\text{dB}}$  are shown in Table I. The CPU time of the proposed PISM takes only 70 s on a computer of Intel Core i7 3.20 GHz CPU and 16 GB of RAM.

### C. RF Amplifier based on TQP7M9103 Chip

The second DUT is a radio frequency (RF) amplifier based on TQP7M9103 chip for a laboratory experiment. Fig. 17 shows a photograph of a PCB containing the RF amplifier and

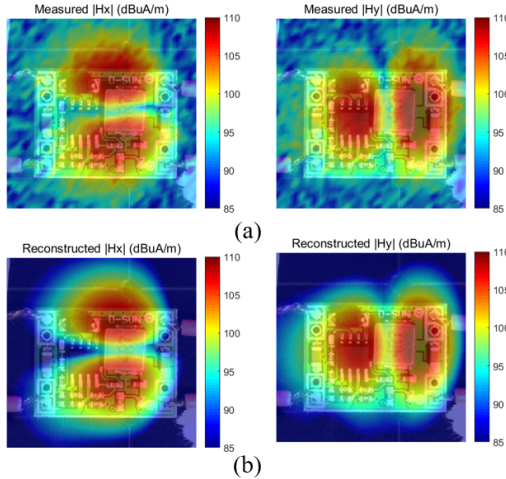


Fig. 15. Magnetic field distributions at 960 kHz on the higher plane ( $z = 11.5$  mm). (a) Measured  $|H_x|$  and  $|H_y|$ . (b) Reconstructed  $|H_x|$  and  $|H_y|$ .

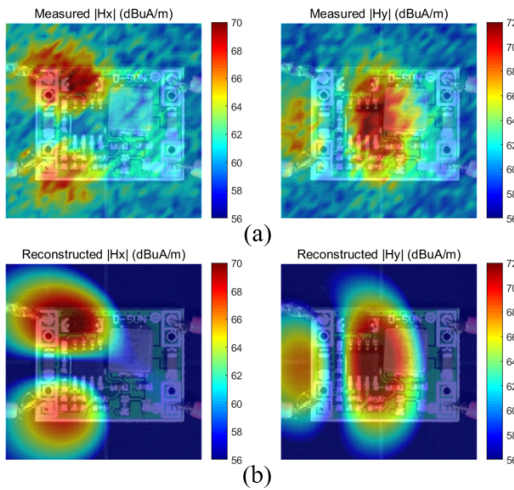


Fig. 16. Magnetic field distributions at 36.2 MHz on the higher plane ( $z = 11.5$  mm). (a) Measured  $|H_x|$  and  $|H_y|$ . (b) Reconstructed  $|H_x|$  and  $|H_y|$ .

TABLE I  
ERRORS FOR FIGS. 15 AND 16

	960kHz		36.2MHz	
	$ H_x $	$ H_y $	$ H_x $	$ H_y $
$\sigma$	22%	21%	37%	36%
$\sigma_{\text{dB}}$	-13.15	-13.56	-8.63	-8.87

TQP7M9103 chip. The length and width of the RF amplifier are 34 and 25 mm, respectively. The RF amplifier based on TQP7M9103 chip provides good linearity from 50 MHz to 4 GHz. In this article, the operating frequency is 1 GHz.

The scanning plane ( $36 \text{ mm} \times 28.5 \text{ mm}$ ) is set at  $z = 7 \text{ mm}$  with 1.5-mm sampling interval ( $\Delta x = \Delta y = 1.5 \text{ mm}$ ). Hence, we have 25 sampling points in the  $x$ -direction and 20 sampling points in the  $y$ -direction. The reconstructed area of the equivalent magnetic current at  $z = 1 \text{ mm}$  is set equal to the area of scanning plane and is divided into  $48 \times 38 = 1824$  elements by a square grid with a side length of 0.75 mm. The grid of source area is finer than that of the scanning plane

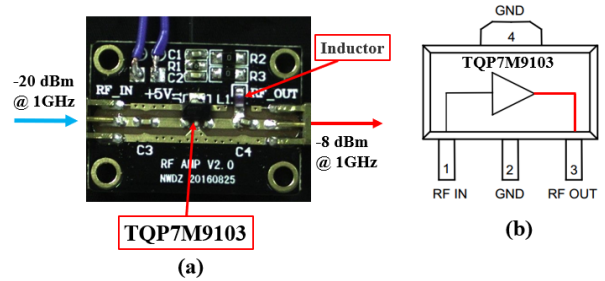


Fig. 17. (a) Top view of RF amplifier. (b) TQP7M9103 chip.

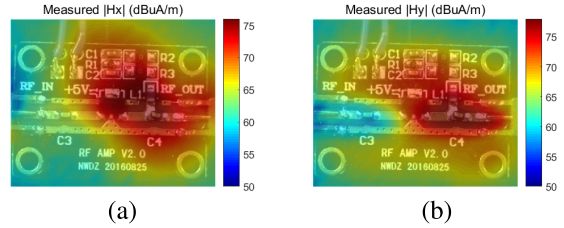


Fig. 18. Magnetic field distributions at 1 GHz on the scanning plane ( $z = 7$  mm). (a) Measured  $|H_x|$ . (b) Measured  $|H_y|$ .

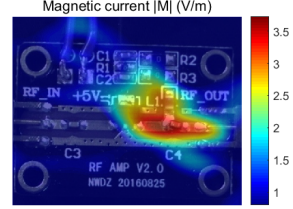


Fig. 19. Equivalent magnetic current  $|M|$  distribution for the RF amplifier.

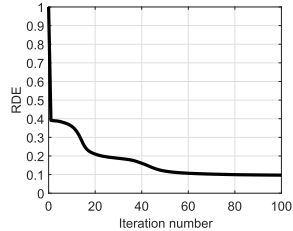


Fig. 20. RDE versus iteration number for the RF amplifier.

to obtain a better resolution and show the good ability of the proposed PISM in solving the underdetermined system.

Magnetic field distributions at 1 GHz on the scanning plane are shown in Fig. 18. The equivalent magnetic current obtained by the proposed PISM is shown in Fig. 19. It can be effectively seen that the equivalent magnetic current is distributed on the output pin of the TQP7M9103 chip, microstrip line, and inductor. The RDE curve is shown in Fig. 20 and finally terminates at about 9.8%. The CPU time of this test is about 5 min.

## VI. CONCLUSION

An efficient PISM based on magnitude-only and single-plane near-field scanning is proposed for radiation source diagnosis and prediction of PCBs. The equivalent source is obtained by using an iterative method to minimize the nonlinear cost function. Numerical and laboratory experiments show that this method is effective and convergent and has good robustness with noise and the amount of measured data.

It should be pointed out that the method proposed in this article can also be applied to the equivalent electric current source reconstruction. Due to the introduction of regularization and the existence of noise, the equivalent source obtained by PISM is not the exact solution but is a reasonable solution close to the true solution.

## REFERENCES

- [1] K. Mainali and R. Oruganti, "Conducted EMI mitigation techniques for switch-mode power converters: A survey," *IEEE Trans. Power Electron.*, vol. 25, no. 9, pp. 2344–2356, Sep. 2010.
- [2] H. H. Park, H.-T. Jang, H.-B. Park, and C. Choi, "An EMI evaluation method for integrated circuits in mobile devices," *IEEE Trans. Electromagn. Compat.*, vol. 55, no. 4, pp. 780–787, Aug. 2013.
- [3] N. Mutoh, J. Nakashima, and M. Kaneko, "Multilayer power printed structures suitable for controlling EMI noises generated in power converters," *IEEE Trans. Ind. Electron.*, vol. 50, no. 6, pp. 1085–1094, Dec. 2003.
- [4] J. Shi, M. A. Cracraft, K. P. Slattery, M. Yamaguchi, and R. E. DuBroff, "Calibration and compensation of near-field scan measurements," *IEEE Trans. Electromagn. Compat.*, vol. 47, no. 3, pp. 642–650, Aug. 2005.
- [5] J.-M. Kim, W.-T. Kim, and J.-G. Yook, "Resonance-suppressed magnetic field probe for EM field-mapping system," *IEEE Trans. Microw. Theory Techn.*, vol. 53, no. 9, pp. 2693–2699, Sep. 2005.
- [6] Y.-T. Chou and H.-C. Lu, "Magnetic near-field probes with high-pass and notch filters for electric field suppression," *IEEE Trans. Microw. Theory Techn.*, vol. 61, no. 6, pp. 2460–2470, Jun. 2013.
- [7] X. Tong, D. W. P. Thomas, A. Nothofer, P. Sewell, and C. Christopoulos, "Modeling electromagnetic emissions from printed circuit boards in closed environments using equivalent dipoles," *IEEE Trans. Electromagn. Compat.*, vol. 52, no. 2, pp. 462–470, May 2010.
- [8] S. M. M. Mirtalaei, S. H. H. Sadeghi, and R. Moini, "A combined method-of-moments and near-field measurements for EMI evaluation of switched-mode power supplies," *IEEE Trans. Ind. Electron.*, vol. 61, no. 4, pp. 1811–1818, Apr. 2014.
- [9] Z. Yu, M. Chai, J. A. Mix, K. P. Slattery, and Q. H. Liu, "Inverse source solver for a high resolution near field scanner in microelectronic applications," *IEEE Trans. Compon., Packag., Manuf. Technol.*, vol. 4, no. 9, pp. 1495–1502, Sep. 2014.
- [10] Y. Alvarez, M. Rodriguez, F. Las-Heras, and M. M. Hernando, "On the use of the source reconstruction method for estimating radiated EMI in electronic circuits," *IEEE Trans. Instrum. Meas.*, vol. 59, no. 12, pp. 3174–3183, Dec. 2010.
- [11] H. Zhao, S. Tao, Z. Chen, and J. Hu, "Sparse source model for prediction of radiations by transmission lines on a ground plane using a small number of near-field samples," *IEEE Antennas Wireless Propag. Lett.*, vol. 18, no. 1, pp. 103–107, Jan. 2019.
- [12] R. R. Alavi, R. Mirzavand, A. Kiaee, R. Patton, and P. Mousavi, "Detection of the defective vias in SiW circuits from single/array probe(s) data using source reconstruction method and machine learning," *IEEE Trans. Microw. Theory Techn.*, vol. 67, no. 9, pp. 3757–3770, Sep. 2019.
- [13] J. A. Russer and P. Russer, "Modeling of noisy EM field propagation using correlation information," *IEEE Trans. Microw. Theory Techn.*, vol. 63, no. 1, pp. 76–89, Jan. 2015.
- [14] R. G. Yacarino and Y. Rahmat-Samii, "Phaseless bi-polar planar near-field measurements and diagnostics of array antennas," *IEEE Trans. Antennas Propag.*, vol. 47, no. 3, pp. 574–583, Mar. 1999.
- [15] S. F. Razavi and Y. Rahmat-Samii, "Resilience to probe-positioning errors in planar phaseless near-field measurements," *IEEE Trans. Antennas Propag.*, vol. 58, no. 8, pp. 2632–2640, Aug. 2010.
- [16] M. M. Hernando, A. Fernandez, M. Arias, M. Rodriguez, Y. Alvarez, and F. Las-Heras, "EMI radiated noise measurement system using the source reconstruction technique," *IEEE Trans. Ind. Electron.*, vol. 55, no. 9, pp. 3258–3265, Sep. 2008.
- [17] Y. Vives-Gilabert, C. Arcambal, A. Louis, F. de Daran, P. Eudeline, and B. Mazari, "Modeling magnetic radiations of electronic circuits using near-field scanning method," *IEEE Trans. Electromagn. Compat.*, vol. 49, no. 2, pp. 391–400, May 2007.
- [18] J. Zhang, K. W. Kam, J. Min, V. V. Khilkevich, D. Pommerenke, and J. Fan, "An effective method of probe calibration in phase-resolved near-field scanning for EMI application," *IEEE Trans. Instrum. Meas.*, vol. 62, no. 3, pp. 648–658, Mar. 2013.
- [19] J. Zhang and J. Fan, "Source reconstruction for IC radiated emissions based on magnitude-only near-field scanning," *IEEE Trans. Electromagn. Compat.*, vol. 59, no. 2, pp. 557–566, Apr. 2017.
- [20] X. Tong, D. W. P. Thomas, A. Nothofer, P. Sewell, and C. Christopoulos, "A genetic algorithm based method for modeling equivalent emission sources of printed circuits from near-field measurements," in *Proc. Asia-Pacific Int. Symp. Electromagn. Compat.*, 2010, pp. 293–296.
- [21] B. Wang, E.-X. Liu, W.-J. Zhao, and C. E. Png, "Reconstruction of equivalent emission sources for PCBs from near-field scanning using a differential evolution algorithm," *IEEE Trans. Electromagn. Compat.*, vol. 60, no. 6, pp. 1670–1677, Dec. 2018.
- [22] C. Wu, Z. Sun, Q. Huang, Y. Wang, J. Fan, and J. Zhou, "A method to extract physical dipoles for radiating source characterization and near field coupling estimation," in *Proc. IEEE Int. Symp. Electromagn. Compat., Signal Power Integrity (EMC+SIPI)*, Jul. 2019, pp. 580–583.
- [23] Y. Alvarez, F. Las-Heras, and M. R. Pino, "The sources reconstruction method for amplitude-only field measurements," *IEEE Trans. Antennas Propag.*, vol. 58, no. 8, pp. 2776–2781, Aug. 2010.
- [24] B. Zitouna and J. B. H. Slama, "Time domain inverse method based on the near field technique to solve electromagnetic interference problems: Application to an AC/DC flyback converter," *IET Power Electron.*, vol. 11, no. 13, pp. 2133–2139, Nov. 2018.
- [25] W. Fan, Z. Chen, and W. J. R. Hoefer, "Source reconstruction from wideband and band-limited responses by FDTD time reversal and regularized least squares," *IEEE Trans. Microw. Theory Techn.*, vol. 65, no. 12, pp. 4785–4793, Dec. 2017.
- [26] Q. Huang and J. Fan, "Machine learning based source reconstruction for RF desense," *IEEE Trans. Electromagn. Compat.*, vol. 60, no. 6, pp. 1640–1647, Dec. 2018.
- [27] Y.-F. Shu, X.-C. Wei, J. Fan, R. Yang, and Y.-B. Yang, "An equivalent dipole model hybrid with artificial neural network for electromagnetic interference prediction," *IEEE Trans. Microw. Theory Techn.*, vol. 67, no. 5, pp. 1790–1797, May 2019.
- [28] L. Li, J. Pan, C. Hwang, and J. Fan, "Radiation noise source modeling and application in near-field coupling estimation," *IEEE Trans. Electromagn. Compat.*, vol. 58, no. 4, pp. 1314–1321, Aug. 2016.
- [29] W. Labiedh and J. B. H. Slama, "Analysis and modeling of the magnetic near fields emitted by an IGBT and by a power diode generic radiating model for active components," in *Proc. Int. Conf. Electr. Sci. Technol. Maghreb (CISTEM)*, Nov. 2014, pp. 1–6.
- [30] R. Nowak and S. Frei, "Reconstruction of current distribution on a given conductor structure using frequency domain near-field data without phase information," in *Proc. Int. Symp. Electromagn. Compat.*, Sep. 2019, pp. 668–673.
- [31] J.-M. Jin, *Theory and Computation of Electromagnetic Fields*. Hoboken, NJ, USA: Wiley, 2011.
- [32] C. A. Balanis, *Advanced Engineering Electromagnetics*. Hoboken, NJ, USA: Wiley, 2012.
- [33] J. Pan *et al.*, "Application of dipole-moment model in EMI estimation," in *Proc. IEEE Int. Symp. Electromagn. Compat. (EMC)*, Aug. 2015, pp. 350–354.
- [34] Z. Yu, J. Zhou, Y. Fang, Y. Hu, and Q. H. Liu, "Through-casing hydraulic fracture evaluation by induction logging II: The inversion algorithm and experimental validations," *IEEE Trans. Geosci. Remote Sens.*, vol. 55, no. 2, pp. 1189–1198, Feb. 2017.
- [35] L. Pan, Y. Zhong, X. Chen, and S. P. Yeo, "Subspace-based optimization method for inverse scattering problems utilizing phaseless data," *IEEE Trans. Geosci. Remote Sens.*, vol. 49, no. 3, pp. 981–987, Mar. 2011.
- [36] C. L. Lawson and R. J. Hanson, *Solving Least Squares Problems*, vol. 15. Philadelphia, PA, USA: SIAM, 1995.
- [37] C. Qiu *et al.*, "Multifrequency 3-D inversion of GRETEM data by BCGS-FFT-BIM," *IEEE Trans. Geosci. Remote Sens.*, vol. 57, no. 4, pp. 2439–2448, Apr. 2019.
- [38] F. Li, Q. H. Liu, and L.-P. Song, "Three-dimensional reconstruction of objects buried in layered media using born and distorted born iterative methods," *IEEE Geosci. Remote Sens. Lett.*, vol. 1, no. 2, pp. 107–111, Apr. 2004.
- [39] M. R. Hestenes and E. Stiefel, "Methods of conjugate gradients for solving linear systems," *J. Res. Natl. Bur. Standards*, vol. 49, pp. 409–436, Dec. 1952.
- [40] (2018). *Wavenology EM*. [Online]. Available: <http://www.wavenology.com/>
- [41] E. Joy and D. Paris, "Spatial sampling and filtering in near-field measurements," *IEEE Trans. Antennas Propag.*, vol. 20, no. 3, pp. 253–261, May 1972.

- [42] J.-C. Zhang, X.-C. Wei, R. Yang, R. X.-K. Gao, and Y.-B. Yang, "An efficient probe calibration based near-field-to-near-field transformation for EMI diagnosis," *IEEE Trans. Antennas Propag.*, vol. 67, no. 6, pp. 4141–4147, Jun. 2019.
- [43] Z. Yan, J. Wang, W. Zhang, Y. Wang, and J. Fan, "A simple miniature ultrawideband magnetic field probe design for magnetic near-field measurements," *IEEE Trans. Antennas Propag.*, vol. 64, no. 12, pp. 5459–5465, Dec. 2016.



**Lixiao Wang** received the B.S. degree in electrical engineering from Beijing Jiaotong University, Beijing, China, in 2016. He is currently pursuing the Ph.D. degree at Xiamen University, Xiamen, China.

His research interests include electromagnetic interference, inverse source problems, electromagnetic imaging by the ground-penetrating radar, and computational electromagnetics.



**Yuxian Zhang** (Student Member, IEEE) received the B.S. and M.S. degrees from the Tianjin University of Technology and Education, Tianjin, China, in 2012 and 2015, respectively, and the Ph.D. degree from the College of Electronic Science and Technology, Xiamen University, Xiamen, China, in 2018.

He is currently an Associate Professor with the Institute of Microscale Optoelectronics, Shenzhen University, China. He has authored or coauthored 25 papers in the refereed journals and the conference proceedings and holds four Chinese patents. His current research interests include subsurface reverse-time migration imaging and computational electromagnetics, especially in the anisotropic finite-difference time-domain (FDTD) method.

Dr. Zhang was a three-time recipient of the Chinese National Scholarship and has participated in the Chinese Graduate Mathematical Contest in Modeling for five times during which he has been bestowed national awards. He has served as a reviewer for three journals.



**Feng Han** (Senior Member, IEEE) received the B.S. degree in electronic science from Beijing Normal University, Beijing, China, in 2003, the M.S. degree in geophysics from Peking University, Beijing, in 2006, and the Ph.D. degree in electrical engineering from Duke University, Durham, NC, USA, in 2011.

He is currently an Assistant Professor with the Institute of Electromagnetics and Acoustics, Xiamen University, Xiamen, China. His research interests include ionosphere remote sensing by radio atmospherics, electromagnetic full-wave inversion by integral equations, reverse time migration image, and the design of an electromagnetic detection system.



**Jianyang Zhou** (Member, IEEE) received the B.Eng. degree in electrical engineering from Xi'an Jiaotong University, Xi'an, China, in 1991, the M.Eng. degree in automation control from Beijing Technology and Business University, Beijing, China, in 1997, and the Ph.D. degree in environmental science from Xiamen University, Xiamen, China, in 2005.

From 1991 to 1994, he was an Assistant Engineer with Xiamen Fuda Photographic Materials Company Ltd., Xiamen. He was a Post-Doctoral Research Fellow with Xiamen Overseas Chinese Electronic Company Ltd., Xiamen, from 2007 to 2009, and the Department of Electrical and Computer Engineering, Duke University, Durham, NC, USA, from 2013 to 2015. Since 2018, he has been a Professor with the Department of Electronic Engineering, Xiamen University. His research interests include computational electromagnetics, numerical methods in acoustic, nanophotonics, and biomedical imaging.



**Qing Huo Liu** (Fellow, IEEE) received the B.S. and M.S. degrees in physics from Xiamen University, China, in 1983 and 1986, respectively, and the Ph.D. degree in electrical engineering from the University of Illinois at Urbana-Champaign, Champaign, IL, USA, in 1989.

He was with the Electromagnetics Laboratory, University of Illinois at Urbana-Champaign, as a Research Assistant, from September 1986 to December 1988, and a Post-doctoral Research Associate from January 1989 to February 1990. He was a Research Scientist and the Program Leader with Schlumberger-Doll Research, Ridgefield, CT, USA, from 1990 to 1995. From 1996 to May 1999, he was an Associate Professor with New Mexico State University, Las Cruces, NM, USA. Since June 1999, he has been with Duke University, Durham, NC, USA, where he is currently a Professor of electrical and computer engineering. He has also been the Founder and the chairman of Wave Computation Technologies, Inc., Durham, NC, USA, since 2005. His research interests include computational electromagnetics and acoustics, inverse problems, and their application in nanophotonics, geophysics, biomedical imaging, and electronic packaging. He has published widely in these areas.

Dr. Liu is a Fellow of the Acoustical Society of America, the Electromagnetics Academy, and the Optical Society of America. He served as the Founding Editor-in-Chief for the *IEEE Journal on Multiscale and Multiphysics Computational Techniques*. He received the 1996 Presidential Early Career Award for Scientists and Engineers (PECASE) from the White House, the 1996 Early Career Research Award from the Environmental Protection Agency, the 1997 CAREER Award from the National Science Foundation, the 2017 Technical Achievement Award and the 2018 Computational Electromagnetics Award from the Applied Computational Electromagnetics Society, the 2018 Harrington-Mittra Award in Computational Electromagnetics from the IEEE Antennas and Propagation Society, and the University of Illinois at Urbana-Champaign ECE Distinguished Alumni Award in 2018. He has served as a Distinguished Lecturer for the IEEE Antennas and Propagation Society.